

AFRL-SR-BL-TR-00-

0306

REPORT DOCUMENTATION PAGE

The public reporting burden for this collection of information is estimated to average 1 hour per response, including gathering and maintaining the data needed, and completing and reviewing the collection of information. Send comments regarding this burden estimate or any other aspect of this collection of information, including suggestions for reducing the burden, to Department of Defense, Washington Headquarters Services, Directorate for Information Operations and Reports (0704-0188), 1215 Jefferson Davis Highway, Suite 1204, Arlington, VA 22202-4302. Respondents should be aware that notwithstanding any other provision of law, no person shall be subject to any penalty for failing to comply with a collection of information if it does not display a currently valid OMB control number.

PLEASE DO NOT RETURN YOUR FORM TO THE ABOVE ADDRESS.

1. REPORT DATE (DD-MM-YYYY) 06-15-2000		2. REPORT TYPE Final Report		3. DATES COVERED (From - To) 01 Sep 96 - 30 Sep 99	
4. TITLE AND SUBTITLE  Shock-induced Damage in Rock and Concrete				5a. CONTRACT NUMBER	
				5b. GRANT NUMBER AFOSR F49620-96-1-0444	
				5c. PROGRAM ELEMENT NUMBER	
6. AUTHOR(S)  Charles Cangli Liu and Thomas J. Ahrens				5d. PROJECT NUMBER	
				5e. TASK NUMBER 2302/CX	
				5f. WORK UNIT NUMBER	
7. PERFORMING ORGANIZATION NAME(S) AND ADDRESS(ES) California Institute of Technology 252-21 1200 E. California Blvd. Pasadena, CA 91125				8. PERFORMING ORGANIZATION REPORT NUMBER	
9. SPONSORING/MONITORING AGENCY NAME(S) AND ADDRESS(ES) AFOSR/NA 801 N. Randolph Street, Room 732 Arlington VA 22203-1977				10. SPONSOR/MONITOR'S ACRONYM(S)	
				11. SPONSOR/MONITOR'S REPORT NUMBER(S)	
12. DISTRIBUTION/AVAILABILITY STATEMENT  Approved for public release; distribution unlimited.					
13. SUPPLEMENTARY NOTES  14. ABSTRACT We have developed a technique for measuring the depth time history of rigid body penetration into brittle materials under a deceleration of $\sim 10^3$ g. A series of 4140 steel projectile penetrations into G-mixture mortar targets has been conducted in the velocity range of 100 to 500 m/s. Based on the experimental results, the target materials are damaged via compacting and brittle radial and lateral crack propagation in front of and surrounding the penetration path. The projectile-target contact length on the projectile lateral surface is $< 20\%$ of final penetration depth. This suggests that the effect of lateral friction on the penetration process can be ignored. Final penetration depth is found to be linearly scaled with initial projectile energy per unit cross-section area. Based on the fact that the penetration duration increases slowly with impact velocity, does not approximately depend on projectile. Deduced penetration velocity-time histories suggest that the whole penetration is divided into three stages: an initial stage, a steady penetration stage and a penetration stop stage. The average deceleration in the steady penetration stage for projectiles with the same dimensions is found to be linearly proportional to initial impact velocity. The average resistance pressure during penetration is estimated to be comparable to shock wave pressure. The present data demonstrate that a very strong similarity of penetration depth-time history is described by a relation between normalized penetration depth and normalized penetration time. This similarity can be used to predict penetration depth-time history under different initial projectile conditions.					
15. SUBJECT TERMS shock damage, rock and concrete, depth time history, rigid body penetration, brittle materials					
16. SECURITY CLASSIFICATION OF:			17. LIMITATION OF ABSTRACT	18. NUMBER OF PAGES	19a. NAME OF RESPONSIBLE PERSON
a. REPORT	b. ABSTRACT	c. THIS PAGE			19b. TELEPHONE NUMBER (Include area code)

# Shock-induced Damage in Rock and Concrete

C. Liu and T. J. Ahrens  
Seismological Laboratory  
California Institute of Technology  
Pasadena, CA 91125

## Final Report

Air Force Office of Scientific Research  
September 1, 1996 to September 30, 1999  
Grant F49620-96-1-0444

20000817 084

# Contents

<b>1</b>	<b>Introduction</b>	<b>5</b>
<b>2</b>	<b>Penetration Depth Time History Measurement Method</b>	<b>6</b>
2.1	Projectile and Sabot Design . . . . .	7
2.1.1	Rigid Body Assumption . . . . .	7
2.1.2	Projectile and Sabot Design . . . . .	7
2.2	Sabot-Projectile Separation System . . . . .	11
2.3	Detection and Recording System . . . . .	12
2.4	Error Analysis . . . . .	13
2.4.1	Intrinsic Time Error during Penetration . . . . .	13
2.4.2	Penetration Depth Uncertainty . . . . .	15
2.5	Experimental Validation of Present Method . . . . .	15
<b>3</b>	<b>Experimental Results and Empirical Scaling Relations</b>	<b>18</b>
3.1	Characterization of G-mixture Mortar . . . . .	18
3.1.1	Ambient Condition Properties . . . . .	18
3.1.2	Mortar Response to Impact Loading . . . . .	18
3.2	Penetration Damage Characterization . . . . .	21
3.2.1	Characteristics of the recovered targets . . . . .	21
3.2.2	Projectile damage pattern . . . . .	26
3.3	Penetration time history data and scaling . . . . .	28
3.3.1	Final penetration depth . . . . .	28
3.3.2	Energy per unit penetration volume . . . . .	30
3.3.3	Effects of target dimension on penetration . . . . .	31
3.3.4	Penetration time history . . . . .	32
3.3.5	Penetration process similarity . . . . .	37
3.4	Comparisons among empirical relations . . . . .	38
<b>4</b>	<b>Conclusions</b>	<b>40</b>

## List of Figures

1	Experiment set-up. . . . .	8
2	Schematic of optical and recording system. . . . .	9
3	Convolution between laser energy and the reflection function. . .	10
4	Three possible patterns of reflected energy variations with time. .	10
5	Sabot and projectile. . . . .	12
6	Schematic of bar-reader. . . . .	14
7	Typical experimental record of reflected laser energy. . . . .	16
8	Configuration for stress wave profile experiments. . . . .	20
9	Stress wave profiles in G-mixture mortar. . . . .	20
10	Unconfined compressive strength versus strain rate. . . . .	22
11	Schematic view of post-shot targets. . . . .	22
12	Damage pattern for Shot 1017. . . . .	23
13	Radial crack length versus impact energy. . . . .	24
14	Crater profiles. . . . .	25
15	Ratio of crater-to-projectile radius versus projectile velocity. . .	25
16	Crater depth versus initial projectile energy. . . . .	26
17	Cross-section of recovered target for Shot 1017. . . . .	26
18	Cross-section of the recovered target for Shot P38. . . . .	27
19	Schematic of cross-section of the target for Shot 1017. . . . .	27
20	Recovered projectiles. . . . .	29
21	Normalized damage length versus final penetration depth. . . . .	29
22	Final penetration depth versus initial energy per unit area. . . .	30
23	Energy per unit penetration volume versus energy per unit area. .	31
24	Penetration depth versus time. . . . .	32
25	Penetration duration versus energy per unit area. . . . .	34
26	Deduced penetration velocity-time history. . . . .	35
27	Deduced deceleration-time history. . . . .	36
28	Average deceleration versus impact velocity. . . . .	36
29	Average pressure normal to projectile surface. . . . .	37
30	Normalized penetration depth versus normalized penetration time. .	38
31	Final penetration depth versus momentum per unit area. . . . .	40
32	Final penetration depth versus energy per unit area. . . . .	41

## List of Tables

1	Penetration experimental parameters. . . . .	17
2	Initial velocity comparison. . . . .	17
3	Ultrasonic velocity and elastic moduli of the mortar. . . . .	18
4	Uniaxial strain impact data of G-mixture mortar. . . . .	19

### Abstract

We have developed a technique for measuring the depth time history of rigid body penetration into brittle materials under a deceleration of  $\sim 10^5$  g. A series of 4140 steel projectile penetrations into G-mixture mortar targets has been conducted in the velocity range of 100 to 500 m/s. Based on the experimental results, the target materials are damaged via compacting and brittle radial and lateral crack propagation in front of and surrounding the penetration path. The projectile-target contact length on the projectile lateral surface is  $< 20\%$  of final penetration depth. This suggests that the effect of lateral friction on the penetration process can be ignored. Final penetration depth is found to be linearly scaled with initial projectile energy per unit cross-section area. Based on the fact that the penetration duration increases slowly with impact velocity, does not approximately depend on projectile. Deduced penetration velocity-time histories suggest that the whole penetration is divided into three stages: an initial stage, a steady penetration stage and a penetration stop stage. The average deceleration in the steady penetration stage for projectiles with the same dimensions is found to be linearly proportional to initial impact velocity. The average resistance pressure during penetration is estimated to be comparable to shock wave pressure. The present data demonstrate that a very strong similarity of penetration depth-time history is described by a relation between normalized penetration depth and normalized penetration time. This similarity can be used to predict penetration depth-time history under different initial projectile conditions.

## 1 Introduction

Although research on rigid body penetration dynamics has taken place for more than a century ([4], [6], and [11]), the penetration process is not well understood as it involves impact-induced shock propagation, crack initiation, friction and propagation, and large plastic deformations that are still the subject of much study. Therefore, experimental method development, and analytical and numerical modeling of the penetration process are still very active topics of research. Rigid body penetration has many applications. Besides power station safety and military applications, the use of rigid penetrators in space exploration is likely to begin in the next several years ([2], [21] and [10]). Proposed applications of rigid penetrators as part of planetary exploration missions include: (1) The Champollion mission ([2]) which will explosively deploy a 3-meter long harpoon to anchor a lander into a comet surface so that other activities may proceed in this low-gravity environment; (2) The Deep Space 2 ([10]), Champollion and the Lunar-A ([21]) missions that are going to use penetrators to emplace various probes into the soil on Mars, a comet and the Moon respectively; and (3) The use of penetration time history to determine planetary material properties. In order for the above applications to be successful, knowledge of the dynamics of penetration for various target materials is very important for both mission success and data interpretation. Previous penetration studies employed different combinations of projectile and target materials in different velocity ranges

([4], [14], [33], [24], and [27]). Most of these experiments were designed to investigate the relations between initial projectile velocity/energy and penetration depth/crater volume. From two-end-point experimental data (initial impact velocity/energy and final penetration depth/volume), many different relations between penetration depth/volume and impact velocity/energy have been proposed to describe rigid body penetration into soils, rocks and concretes ([4], [7], [13], [33], [14], and [33]). The advantage of empirical relations is that they can be used to predict penetration depth with high reliability under conditions similar to the experimental conditions. The main disadvantage is that they give very limited information about the dynamics during penetration. For a single set of experimental data, many different formulae can be used to fit the set ([13]). Therefore, it is difficult to determine which relation is more reasonable than the others. In order to study penetration dynamics, a number of researchers ([19], [22], [15], [28], [8], and [32]) have attempted to measure penetration depth, velocity, and deceleration time history during penetration. The measurement methods employed include: High-speed photography to measure penetration depth-time history ([19], [22] and [32]); Laser Doppler anemometry to determine projectile velocity-time history ([31]); On-board accelerometers to record deceleration time history ([15], [28], and [8]); and Reversed experiments to measure strain, stress and particle velocity in projectile materials ([5]). The understanding of rigid penetration into various soft materials (soils, clays, sands and soft rocks like tuff) has been improved using on-board instrument measurements combined with numerical simulation ([4], and [13]) because of low resistance force and no crack generation during penetration. However, for high-strength brittle materials such as hard rocks, low temperature ice and various concretes, the knowledge of rigid penetration dynamics is still deficient because of the lack of proper methods to measure penetration depth and/or velocity and/or deceleration time history due to very high decelerations. Therefore, in addition to the practical applications, it is important to develop measurement methods that can provide the time history of penetration into brittle materials, and to understand the relations among material properties and time histories. In the following, we first report the method that was developed to measure the depth time history of rigid penetration into brittle materials, and then report the experimental results of penetration into G-mixture mortar targets using the method.

## 2 Penetration Depth Time History Measurement Method

The basic principle of the present method is that if the projectile body is assumed to be rigid during penetration, the time history of the projectile position relative to any point that is stationary relative to the target is identical to the projectile penetration depth-time history into the target. If the penetration depth-time history is measured with very dense points, the projectile penetra-

tion velocity can be deduced by differentiating the time history. The present method includes three crucial elements: (1) Projectile and sabot; (2) Sabot-projectile separator; and (3) Detection and recording system. Figure 1 gives the experimental arrangement inside the 40 mm gun tank at Caltech. Figure 2 shows the optical system. The following is the detailed discussion of the three elements.

## 2.1 Projectile and Sabot Design

### 2.1.1 Rigid Body Assumption

The rigid body assumption is crucial for the validity of the technique to measure penetration depth-time history. Therefore, it is necessary to explore the velocity range that supports the assumption. As an example, the projectile material is chosen to be 4140 steel and the target material is G-mixture mortar (the material properties are discussed in detail in Section 3). Based on the Hugoniot relations of the two materials ([23] and [20]), it is estimated that the projectile body is subject only to elastic deformation for penetrations with an initial impact velocity below 400 m/s.

### 2.1.2 Projectile and Sabot Design

In this method, a projectile body is basically used as a ruler to measure penetration depth. Black and white stripes are put on the projectile lateral surface as labels. In order for the label method to work accurately, two issues that must be considered are the stripe width and strip integrity during launch.

**Optimal Stripe Width** Stripe widths are very important because they affect both temporal and spatial measurement accuracy. However, there are some limitations imposed by machining and the detection system. In order to determine the optimal stripe width under various limitations, we first discuss the relationship between stripe width and reflected laser energy.

Total laser energy reflected from the projectile surface depends on the reflectivity of the projectile surface, the ratio of stripe width to laser beam width, and the intensity profile of incident laser beam energy. When a projectile with a black-and-white striped surface moves across a laser beam, laser energy reflected from the surface is a convolution integral between the incident laser beam intensity profile and projectile surface reflectivity function as illustrated in Figure 3. We approximate the incident laser beam's intensity profile,  $E(x)$ , using a parabolic function, as

$$E(x) = E_0 x(L_l - x), \quad 0 < x < L_l, \quad (1)$$

$$E(x) = 0, \quad x \leq 0; x \geq L_l, \quad (2)$$

where  $x$  is defined in Figure 3,  $L_l$  is the diameter of the incident laser beam and  $E_0$  is a constant. The surface reflectivity function,  $B(x)$ , is  $R_b$  and  $R_w$  for black and white stripes, respectively. Therefore, the total reflected laser energy,



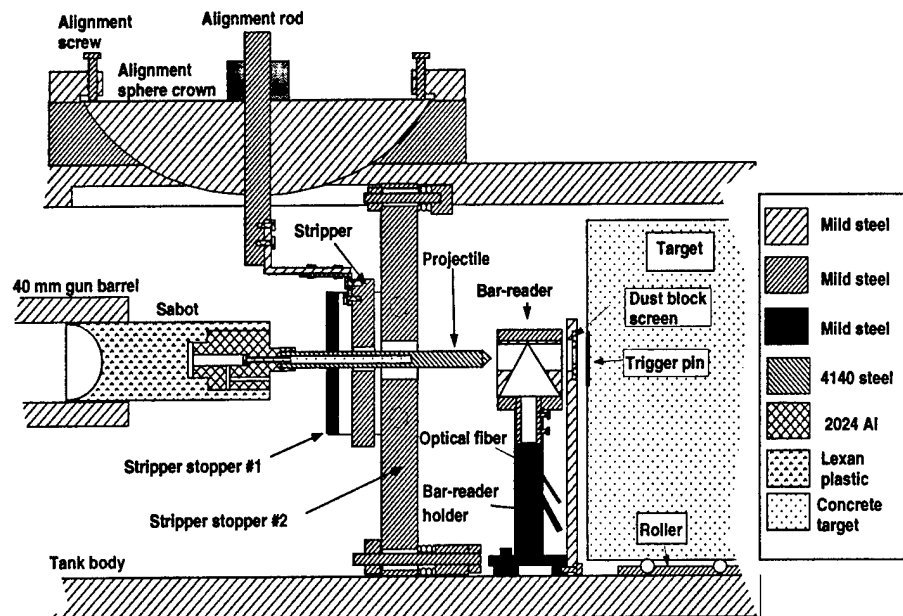


Figure 1: Experiment set-up. Stripper and bar-reader are aligned with the axis of the 40 mm gun barrel using a laser beam that is along the gun barrel axis. Stripper stopper #1 is used to protect the barrel from the impact of a stripper that bounces back after it strikes stripper stopper #2. Stripper stopper #2 is designed to prevent the stripper and sabots from following the projectile and also to prevent gun dust from interfering with the bar-reader during measurement. The recording system is triggered by a pin attached to the impact surface. The trigger pin consists of two copper foils (0.1 mm) that are insulated using a layer of mylar film (0.1 mm). The target (0.5 m diameter and 0.4 - 0.6 m long) sits on a roller and is fixed to the tank body after it is aligned with the gun. Typical distance between the bar-code reader and target surface is ~2 cm. The distance between the bar-reader and the stripper is longer than the projectile length.

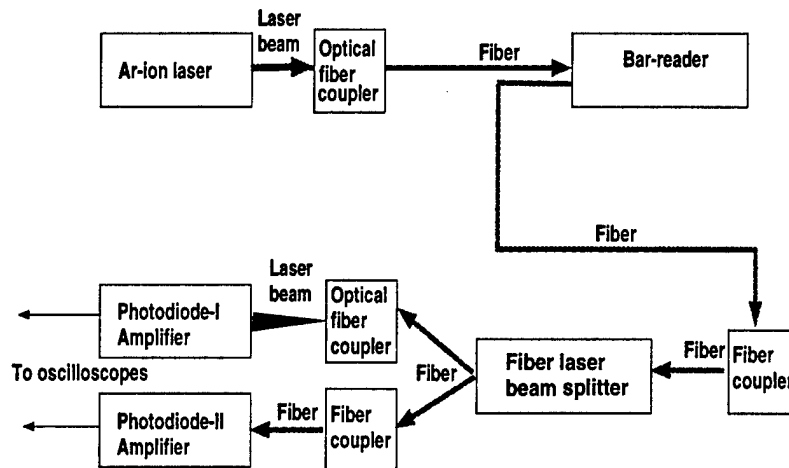


Figure 2: Schematic of optical and recording system. Ar-ion laser is Model 95 (Lexel Laser, Inc.) with a maximum output of 3 W. Laser power used in the present experiments is about 0.7 W. Laser energy is coupled into a  $50\text{ }\mu\text{m}$  core diameter optical fiber using a microlens (F915T, Newport). Fiber from the bar-code reader to the photodiodes is plastic fiber with a core diameter of 2 mm (DuPont). A one-to-two fiber beam splitter is used to distribute laser energy to the two photodiodes. Photodiode-I with a  $20\text{ mm}^2$  sensitive area is C30833 (RCA). The bandwidth of Photodiode-I and amplifier is from 0.004 to 5 MHz. Because it has a very large sensitive area, an optical lens is used to enlarge the diameter of the laser beam from the fiber to fill the entire sensitive area. Photodiode-II with a  $0.8\text{ mm}^2$  sensitive area is C5331-11 (Hamamatsu). The bandwidth of Photodiode-II and its amplifier (APD module, Hamamatsu) is from 0.01 to 80 MHz. Laser energy from the fiber is directly coupled into Photodiode-II.

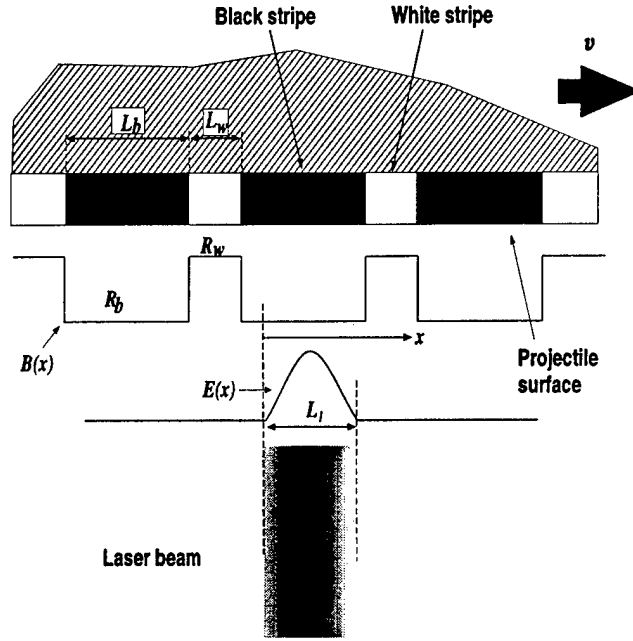


Figure 3: Convolution between laser energy and the reflection function.

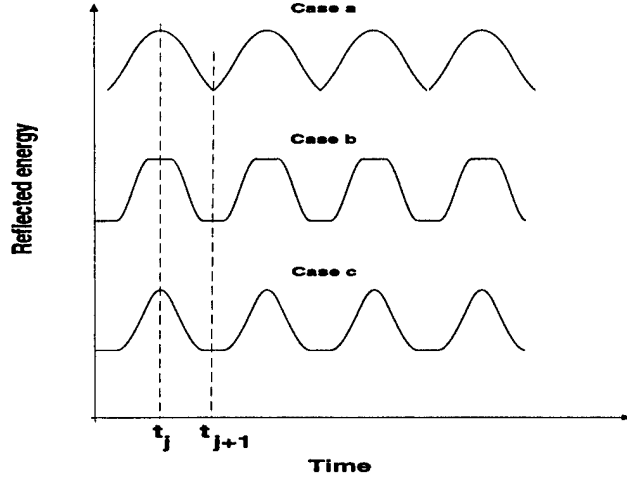


Figure 4: Three possible reflected energy variations with time. For Case A,  $L_l = L_w = L_b$ ; For Case B,  $L_l < L_w, L_l < L_b$  and therefore  $L_l < (L_w + L_b)$ ; For Case C,  $L_w < L_l < L_b$  and  $L_l < (L_w + L_b)$ .  $t_j$  and  $t_{j+1}$  indicate the times at which the centers of the  $j$ th white stripe and  $(j + 1)$ th black stripe pass the center of incident laser beam, respectively.

$E_r$ , at any given time is  $E_r = B(x) * E(x)$ , in which  $*$  specifies the convolution of two functions. This will vary with time depending on the velocity of the projectile surface containing the stripes.

Figure 4 shows three possible scenarios with three different stripe width configurations. From Figure 4 it is seen that time resolution is the highest when  $L_l = L_w = L_b$ . However, due to deviations in assumed projectile distance from the laser beam focal surface and difficulties in consistently machining accurate stripe widths, it is more practical to choose  $L_w < L_l < L_b$ . Under this condition, all peaks in reflected laser energy time series correspond to the moments at which the center of the incident laser beam hits the center of a white stripe. Therefore, optimal stripe width is determined based on incident laser beam diameter. Because the VISAR probe (FOP-1000, Valyn International) that is used to focus the incident laser beam on the projectile surface has a focal diameter of  $< 0.6$  mm, the actual widths chosen for the experiments are  $0.3 \pm 0.05$  mm for white stripes and  $0.7 \pm 0.05$  mm for black stripes.

**Sabot Design** Previous methods used to launch projectiles with large length-to-diameter ratios were either to encapsulate a projectile inside plastic sabots ([14]) or to attach two separate sabots to a projectile by engaging screw threads that cut into the front-most and rear-most portion of the projectile ([3]). These methods damage stripes during launch and sabot-projectile separations. In order to launch projectiles without any damage to the stripes, the projectiles are designed to be held by a combination sabot that consists of aluminum and plastic sabots as shown in Figure 5. The aluminum sabot is used to prevent the projectile from penetrating into the plastic sabot during launch. It also prevents the plastic sabot from following the projectile during and after sabot-projectile separation. Most importantly upon machining the projectile-sabot assembly, it is crucial to ensure that the projectile axis aligns with the sabot axis. A misalignment will result in experiment failure. In order to retain the alignment, an 8 mm long hollow cylinder is used to assure that the projectile axis is aligned with the sabot axis, and a plastic screw is used to tighten them together.

## 2.2 Sabot-Projectile Separation System

In order to conduct penetration measurements free of interference from sabot impact effects, it is necessary to separate the sabots from the projectile immediately after they exit the gun barrel. The key issue in the design of the sabot-projectile separation system is to ensure that the separation process does not disturb the projectile trajectory and has a minimal effect on projectile velocity. This appears to be more important for low velocities ( $10^2$  m/s). The sabot-projectile separation system used in this work is shown in Figure 1. Because projectile velocity is relatively low, separation takes a relatively long time, which means that asymmetries in the stripper assembly must be properly considered. Otherwise, reflected waves from the stripper edges may influence the projectile trajectory. The two criteria used to design the stripper are: (1) minimum stripper plate thickness is determined so that sabots should not plug the stripper plate after they impact the stripper; and (2) stripper plate diameter

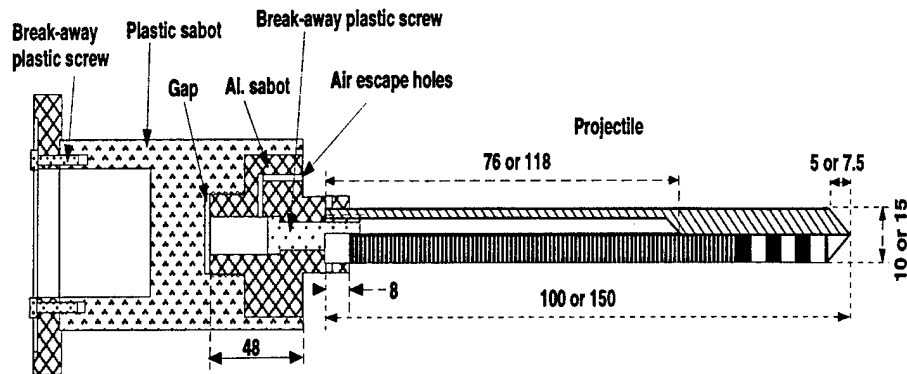


Figure 5: Schematic of the designed sabot-projectile. The black-and-white striped pattern is affixed to the projectiles in the present study. All dimensions are in mm. The stripes near the projectile head are wider to save machining time because this part only provides initial projectile velocity.

must be estimated to be large enough so that waves reflected back from the plate edge do not interfere with the separation process, i.e., that asymmetry on the plate edge will not affect projectile trajectory. Based on these two criteria, the stripper plate dimensions were designed to be 20 mm in thickness and 140/200 mm in diameter for an initial impact velocity that was higher/lower than 200 m/s for a stripper material of #20 steel.

### 2.3 Detection and Recording System

The last issue related to the measurement method is how to detect the projectile position during the penetration process. A stationary laser beam is used to detect the position of a projectile with black and white stripes during its penetration into the target materials. The system used by [3] to measure free-fall projectile velocity in the range of 0-20 m/s is not applicable for penetration depth-time history measurements because the system has a spatial uncertainty of 5 mm and a time resolution of 0-10 kHz. In order to detect all stripes passing over a laser beam with high enough time and spatial resolution, the detection system must collect reflected laser energy very efficiently. Three major factors that affect laser energy collection are: (1) because the bar-coded projectile surface is finished by taking a final light cut on the paint, laser energy reflected from the surface is not spatially uniform; (2) because of possible misalignment of the projectile trajectory from its assumed position, the direction of maximum reflected laser energy may vary with time during penetration, and (3) dust particles from impact and burned propellant products may obscure both the incident

and reflected laser beams if they enter the bar-reader. Based on the above factors, a VISAR probe (FOP-1000, Valyn International) was chosen to focus the incident laser beam on the projectile surface and to collect reflected laser energy (Figure 6). The VISAR probe has a small focal diameter ( $<0.6$  mm) and long field depth ( $\sim 12$  mm), and effectively collects reflected energy from diffusive surfaces when the probe is well aligned with the target surface. However, in the present experiments, the projectile surface is not a good diffusive surface, and possible misalignment exists. In order to overcome this problem, the designed system includes: (1) a well protected and enclosed optical path (Figures 2 and 6), with the only open optical path ( $\sim 5$  mm) between the projectile surface and the surface of a hollow cylinder that the projectiles pass through; (2) laser trap #1, used to reflect part of the laser energy from misaligned and/or non-diffusive surfaces back to the probe; (3) laser trap #2, designed to reflect part of the laser energy focused outside the laser-out plastic fiber back to the fiber; (4) original 1 mm diameter plastic fiber replaced with 2 mm diameter plastic fiber (DuPont), to increase laser collection efficiency (in principle, one can replace it with even larger diameter plastic fibers. However, the low flexibility of plastic fibers with diameters larger than 2 mm results in installation difficulties); and (5) a rubber screen at the end of the hollow cylinder near the impact site, used to block dust particles from entering the hollow cylinder (Figure 1).

During penetration, projectile velocity varies from the initial impact velocity ( $10^2$  m/s) to very low velocity (10 m/s). This large velocity change requires the recording system to have a wide bandwidth. Assuming that initial projectile velocity ranges from 100 to 400 m/s, the time duration between two adjacent reflected laser energy peaks will vary from 2.5 to 10  $\mu$ s during initial penetration. When penetration approaches final depth, projectile velocity is  $\sim 30$  m/s, and the time duration is then  $\sim 35$   $\mu$ s. In general, at least 12 sample points per cycle are needed to accurately record the laser energy profile with a digital oscilloscope or a transient recorder. This means that the sampling rate must be at least 20 MHz. The penetration process lasts about  $10^2$   $\mu$ s. Therefore, the detection system must have a bandwidth of at least 10 kHz to 20 MHz. Based on the above estimation, two different kinds of photodiodes with built-in amplifiers were chosen. One has a bandwidth from 10 kHz to 80 MHz and the other from 4 kHz to 5 MHz. Detailed information on the two photodiodes is given in the caption of Figure 2.

## 2.4 Error Analysis

### 2.4.1 Intrinsic Time Error during Penetration

The intrinsic time error comes from stripe width uncertainty and the rigid body assumption. The contributions from each are estimated as follows:

(1) Error from stripe width uncertainty: The boundary between black and white stripes does not necessarily have a sharp and straight edge due to the machining method adopted, but instead could be diffuse and wavy. This results

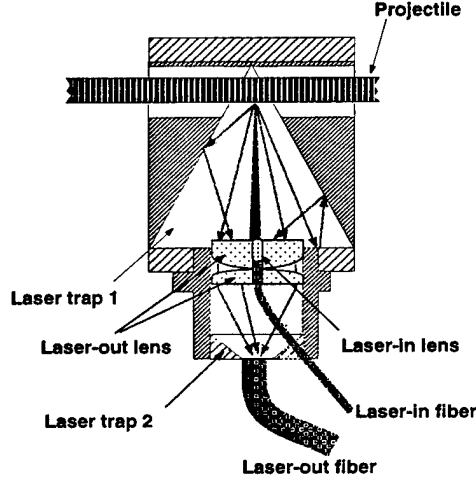


Figure 6: Schematic of bar-reader. (a) is side-section view and (b) is end-section view. All dimensions are in mm.

in a timing error of

$$\delta t_1 = \frac{L_{wb}}{v}, \quad (3)$$

where  $L_{wb}$  is the average boundary width and  $v$  is the projectile velocity.

(2) Error from the rigid body assumption: Elastic waves generated from the initial impact reverberate in the projectile body. This wave reverberation changes the effective stripe width due to strain associated with elastic waves. Assuming that the average stress amplitude of finite elastic wave is  $\sigma_e^a$ , the particle velocity,  $u_e^a$ , related to the elastic wave is

$$u_e^a = \frac{\sigma_e^a}{\rho_p C_e}, \quad (4)$$

where  $\rho_p$  and  $C_e$  are projectile material density and longitudinal elastic wave velocity, respectively. The maximum width change of one pair of black and white stripes induced by the elastic wave is, therefore,

$$\delta L = (L_w + L_b) \frac{u_e^a}{C_e}. \quad (5)$$

The time error,  $\delta t_2$ , related to the width change is

$$\delta t_2 = \frac{\delta L}{v} = \frac{(L_w + L_b)}{v} \frac{u_e^a}{C_e}. \quad (6)$$

Therefore, the maximum possible time error during the penetration process is given by a summation of Eqs. (3) and (6) as

$$\delta t = \delta t_1 + \delta t_2. \quad (7)$$

Then, the relative intrinsic time error, *Error*, is

$$Error = \frac{100\delta t}{(L_w + L_b)/v} = 100\left(\pm \frac{u_e^a}{C_e} \pm \frac{L_{wb}}{L_w + L_b}\right). \quad (8)$$

Using Eq. (8), the time error just after impact can be estimated. For the experiments conducted, the typical values of  $L_w + L_b$ ,  $L_{wb}$  and  $v$  are 1 mm, 0.01 mm and 200 m/s, respectively.  $C_e$  is 5.3 km/s for 4140 steel ([20]). Elastic wave amplitude is taken to be approximately 50% of the peak pressure just after impact, or  $\sigma_e^a = 0.4$  GPa, the measurement point is far away from the impact site ( $\sim 20$  mm). From Eq. (8), the maximum relative error is estimated to be  $\sim 3\%$ . Because the effect of elastic waves can be ignored long after impact, the maximum relative error long after impact is also calculated to be  $\sim 3\%$ .

#### 2.4.2 Penetration Depth Uncertainty

Although a trigger pin is used to give the exact time at which a projectile starts to penetrate into a target, the projectile position is not determined precisely because of the finite stripe width (this is also true for penetration stop point). Therefore, the maximum uncertainty of the positions at which a projectile starts and stops penetrating is half of either the black or white stripe width, depending on where the laser beam hits at that particular moment. Therefore, the maximum uncertainty of the penetration start and stop point ranges from 0.15 to 0.35 mm.

### 2.5 Experimental Validation of Present Method

Using the designed systems and 40 mm gas/powder gun at Caltech, a series of experiments was conducted. Typical reflected laser energy variation recorded is shown in Figure 7 (experimental data on penetration depth time history are shown in Figure 24). Experimental results demonstrate that the systems operated successfully. The validity of the experimental results is demonstrated by the following facts:

(1) Final penetration depth: Table 1 compares the final penetration depth determined by the penetration depth-time measurement with that measured from the recovered targets. The two depths are in good agreement, clearly demonstrating that the present method gives the whole penetration depth-time history.

(2) Initial projectile velocity: The initial projectile velocity was determined using laser obstruction and the X-ray-method. Because projectiles passed through the bar-reader before they started to penetrate into the targets, the initial impact velocity after projectile-sabot separation also was measured by the present method. The good agreement among the three measured velocities (Table 2) shows that the separation system does not affect projectile velocity.



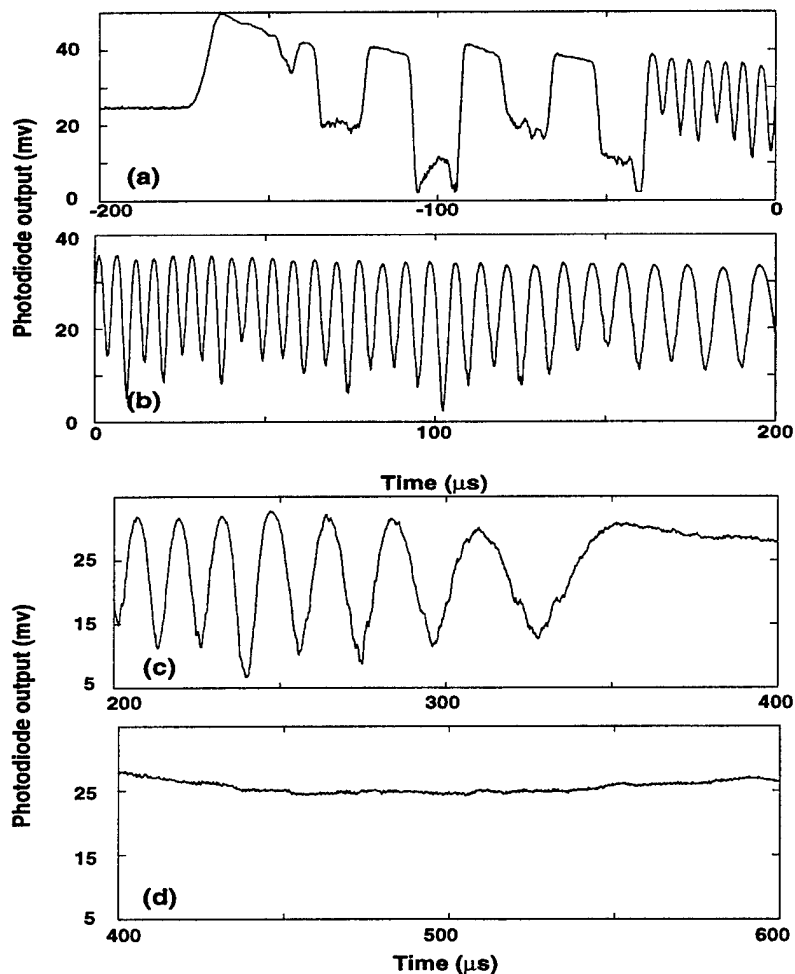


Figure 7: Typical experimental record of reflected laser energy for Shot 1033. Time reference point 0 is from the trigger pin attached to the impact surface and represents the start point of penetration. Figure (a) is photodiode output before the projectile impacted the target. The several wide fringes in Figure (a) are the result of detecting the wider stripes near the projectile tip. Figure (b) gives the record in the first 200  $\mu\text{s}$  after the impact. Figures (c) and (d) show records from 200 to 400, and 400 to 600  $\mu\text{s}$ , respectively, after the impact. Starting at  $t = 350\mu\text{s}$ , it appears that the projectile did not move at all.

Table 1: Penetration experimental parameters.

Shot #	Projectile length (mm)	Projectile diameter (mm)	Projectile mass (gram)	Projectile velocity (m/s)	Penetration depth (mm)	Penetration duration ( $\mu$ s)	Crater depth (mm)
P38	150.0	9.96/9.95	67.5	178.0	30.2 $\pm$ 0.5/30.4 $\pm$ 0.3	327.1 $\pm$ 3	10.5 $\pm$ 2
1017	101.0	9.76/9.69	44.5	272.5	41.4 $\pm$ 1/42.2 $\pm$ 0.3	240 $\pm$ 6	13.6 $\pm$ 2
1018	150.0	10.01/9.65	64.2	505	179.5 $\pm$ 10/		
1033	151.0	10.02/	66.3	213.3	40.5 $\pm$ 0.6/40.3 $\pm$ 0.7	350.1 $\pm$ 3	13.5 $\pm$ 2
1034	151.0	9.99/9.86	66.3	321.1	66.7 $\pm$ 1/65.2 $\pm$ 0.7	385.8 $\pm$ 3	26.4 $\pm$ 4
1035	149.8	15.03/14.98	158.6	313.1	78 $\pm$ 5/	403 $\pm$ 49	
1036	150.0	15.03/15.00	157.6	272.6	55.2 $\pm$ 1/	371 $\pm$ 49	

Measurement error is  $\pm 0.1$  mm for projectile length and  $\pm 0.01$  for projectile diameter,  $\pm 0.1$  grams for mass. Velocity error is given in Table 2. Projectile diameter is given in initial diameter/post-shot diameter. Penetration depth is given in penetration depth<sup>(1)</sup>/penetration depth<sup>(2)</sup>. Penetration depth<sup>(1)</sup> is measured in recovered targets. Error of depth<sup>(1)</sup> comes from smoothness of target surface. Penetration depth<sup>(2)</sup> is given by the penetration depth-time history measurement. Error of depth<sup>(2)</sup> is determined by the width of the stripe that the laser beam was focused on when penetration stopped.

Table 2: Comparison among the three velocities measured.

Shot #	P38	1017	1033	1034	1035	1036
V <sup>(1)</sup>	178.0 $\pm$ 0.1	272.5 $\pm$ 0.3	213.3 $\pm$ 0.5	321.4 $\pm$ 3.0	313.1 $\pm$ 1.9	272.6 $\pm$ 1.9
V <sup>(2)</sup>	172.2 $\pm$ 1.0	265.7 $\pm$ 2.3	215.4 $\pm$ 0.7	320.5 $\pm$ 2.1	309	271
V <sup>(3)</sup>	176.3	269.4				

V<sup>(1)</sup> (m/s) is projectile velocity obtained from present method. V<sup>(2)</sup> (m/s) is projectile velocity given by laser obstruction method. Error is determined from the difference between the two velocities that were given by three laser beams used. Only one velocity was obtained for Shots 1035 and 1036. V<sup>(3)</sup> (m/s) is projectile velocity given by X-ray method that only provided the velocity for Shots P38 and 1017.

Table 3: Ultrasonic velocity and elastic moduli of the mortar.

$\rho_0$ (g/cm <sup>3</sup> )	$C_p$ (km/s)	$C_s$ ( km/s)	$C_b$ (km/s)	$\nu$
1.95±0.02	3.89±0.05	2.22±0.04	2.96±0.03	0.258±0.004
$E$ (GPa)	$G$ (GPa)	$K$ (GPa)	$\sigma_f$ ( GPa)	
24.4±1.1	9.7±0.4	16.8±0.5	0.044	

$\sigma_f$  is unconfined compressive strength at a strain rate of  $2.2 \times 10^{-6} \text{ s}^{-1}$  ([29]). All samples used for compressive strength and velocity measurements were poured together.

### 3 Experimental Results and Empirical Scaling Relations

Using the Caltech 40 mm gas/powder gun, two different kinds of experiments were conducted. The first characterized target material properties using an ultrasonic method and a piezoresistance stress gauge ([17]). The second measured the depth time history of rigid body penetration into a G-mixture mortar target. The projectile material was a heat-treated 4140 steel with  $R_c = 45$  (Rockwell C). The target material was a G-mixture mortar provided by the U.S. Air Force at Tyndall (AFB), Florida ([29]). The mortar targets were 500 mm in diameter and 400/600 mm in length. In order to determine initial properties of the mortar, several cylinders with 150 mm diameter and 300 mm length were made at the same time. The average aggregate size in the mortar was about 0.5 mm and the maximum diameter was less than 2.4 mm ([29]).

#### 3.1 Characterization of G-mixture Mortar

##### 3.1.1 Ambient Condition Properties

The elastic moduli of the mortar were determined by measuring ultrasonic wave velocities using 1 MHz P- and S-wave transducers (Model V153 for S-wave and Model V103 for P-wave, Panametrics, Inc.). The sample preparation procedures are described in detail by [26]. The wave velocities measured are listed in Table 3. The elastic properties of the mortar are calculated from

##### 3.1.2 Mortar Response to Impact Loading

The shock loading data for several concretes and mortars show that there is no substantial difference in the low pressure range (shock wave peak pressure  $< 3$  GPa) ([17]). In order to find out which concrete's or mortar's Hugoniot relation can be used to approximate the G-mixture mortar, two uniaxial strain shock loading experiments were conducted using embedded manganin gauges to measure shock wave profiles at different locations from the impact surface in the stress range of interest. The experimental set-up is given in Figure 8. Figure 9

Table 4: Uniaxial strain impact data of G-mixture mortar.

Shot Num.	$V_p$ (m/s)	Gauge Num.	$h_g$ (mm)	$C_e$ (km/s)	$\sigma_{hel}$ (GPa)	$\sigma_r$ (GPa)	$\sigma_p$ (GPa)	$D$ (km/s)
P40	211	1	5.2	4.32	0.141	0.244	1.14	1.8
		2	10.54	4.32	0.134	0.222	0.94	1.8
P41	227	2	6.67	4.2	0.136	0.245	1.26	1.75

$V_p$  is flyer velocity. Flyer material is tungsten with initial density 19.19 g/cm<sup>3</sup>. The flyer dimensions are 32 mm diameter and 4 mm thickness.  $h_g$  is distance of gauge from impact surface.  $\sigma_r$  is ramp wave peak amplitude and  $\sigma_p$  is shock wave peak pressure.

shows stress profiles from the two experiments. The experimental parameters and results are listed in Table 4. The recorded stress wave profiles in the mortar show that the response of the mortar under uniaxial strain impact loading is divided into two stages: (1) Elastic deformation stage: The elastic wave has an amplitude of  $0.137 \pm 0.004$  GPa and a wave velocity of  $4.26 \pm 0.06$  km/s. Up to a peak shock stress of  $\sim 1$  GPa, a ramp wave forms with an amplitude of  $0.1 \pm 0.01$  GPa; and (2) Plastic deformation stage: Under the experimental conditions, the shock wave propagates at a velocity ( $\sim 1.8$  km/s) that is below the initial bulk wave velocity ( $\sim 2.96$  km/s), with a rise time of 1.2 to 1.6  $\mu$ s upon propagation through a  $\sim 5$  to 10 mm thick sample. All these results reflect large compression in the mortar, i.e., densification. These characteristics were observed in previous work on concrete and mortar ([23] and [12]). The relation of [23] is found to yield shock wave velocity that is in good agreement with the present measurements. Therefore, we assumed that the Hugoniot relation of [23] approximately describes the shock wave equation of state of the G-mixture mortar as

$$D = \begin{cases} 2250 - 3.33v, & v < 150 \text{ m/s}, \\ 900 + 5.17v - 0.00222v^2, & 150 < v < 1300 \text{ m/s}, \end{cases} \quad (9)$$

where  $D$  and  $v$  are shock wave and particle velocity, respectively.

**Compressive Strength** Material compressive strength is one of the important parameters for penetration. Material strength (compressive and tensile) depends on strain rate. [16] found that mortar compressive strength increases dramatically with strain rate. Their experimental data taken with a testing machine (one-dimensional stress) show that the ratio of mortar compressive strength at a strain rate of  $10^{-2}$ /s, to initial strength at a strain rate of  $10^{-7}$ /s,

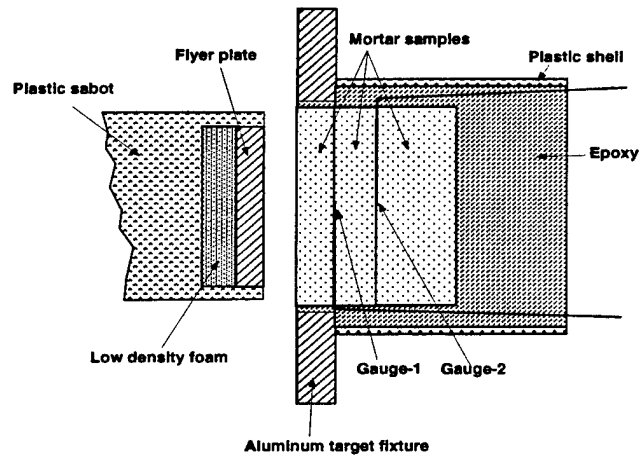


Figure 8: Configuration for stress wave profile experiments. Manganin gauge used is Mn4-50-EK (Dynasen, Inc.); power supply for manganin gauges is CK2 (Dynasen, Inc.).

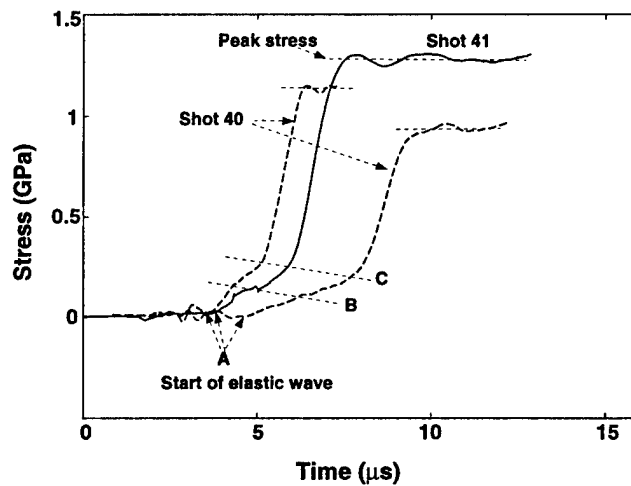


Figure 9: Stress wave profiles in G-mixture mortar. Point A to Point B: elastic wave. Point B to Point C: dispersive elastic wave (ramp wave). Beyond Point C: shock wave. From the wave profiles, we see the decay of elastic, ramp and shock waves with propagation distance.

is approximately 1.9 (Figure 10). Based on previous work on concrete and mortar ([25]), a best fit to the low-strain-rate data of [16] yields

$$\frac{\sigma_f}{\sigma_f^0} = \exp(0.095(\log(\frac{\dot{\epsilon}}{\dot{\epsilon}_0}))^{1.14}), \quad (10)$$

where  $\sigma_f^0$  is compressive strength at strain rate  $\dot{\epsilon}_0 = 2.8 \times 10^{-7}/s$ .

From the uniaxial strain shock loading experiments, yield stress is deduced using ([1])

$$\sigma_y = \frac{\sigma_{hel}}{\frac{K}{2G} + \frac{2}{3}}. \quad (11)$$

Strain rate,  $\dot{\epsilon}$ , at the Hugoniot elastic limit (HEL) is estimated using

$$\dot{\epsilon} \sim \frac{v_e}{C_e \delta t}, \quad (12)$$

where  $v_e$  is the particle velocity at the HEL and  $\delta t$  is the elastic wave rise time. Based on the wave profiles shown in Figure 9 and elastic moduli given in Table 3,  $\sigma_y$  is calculated to be 0.09 GPa at  $\dot{\epsilon} \sim 4 \times 10^3/s$ . In order to approximately estimate compressive strength under shock loading, the ratio of compressive strength to yield stress under uniaxial stress,  $\sim 1.5$  ([16]), is used to deduce a compressive strength of 0.13 GPa. This is about 3 times the compressive strength at the quasi-static strain rate of  $2.2 \times 10^{-6}/s$  measured by [29]. The two experimental data on the G-mixture mortar are plotted in Figure 10, which demonstrates that the results from the uniaxial strain shock and quasi-static loading experiments are in good correlation with the low-strain-rate data from [16]. Therefore, the G-mixture compressive strength during penetration can be estimated using Eq. (10) because the strain rate during penetration is near the strain rate at the HEL.

### 3.2 Penetration Damage Characterization

Table 1 lists the experimental parameters. In this part, the features of penetration damage of targets and projectiles are described based on the observations of recovered targets and projectiles. For convenience later in the discussion, crater depth is defined as the depth generated from spallation process near impact surface, and penetration depth is defined as the distance from the impact surface to the final position of the projectile tip (Figure 11).

#### 3.2.1 Characteristics of the recovered targets

For Shots 1017, 1033 and 1034, projectiles were embedded inside recovered targets. For Shots P38, 1018, 1035 and 1036, projectiles bounced off the recovered targets because final penetration depth was small for Shots P38 and 1036, and the targets were broken for Shots 1018 and 1035. Figure 11 is a general schematic view of a post-shot target with embedded projectile. We observed

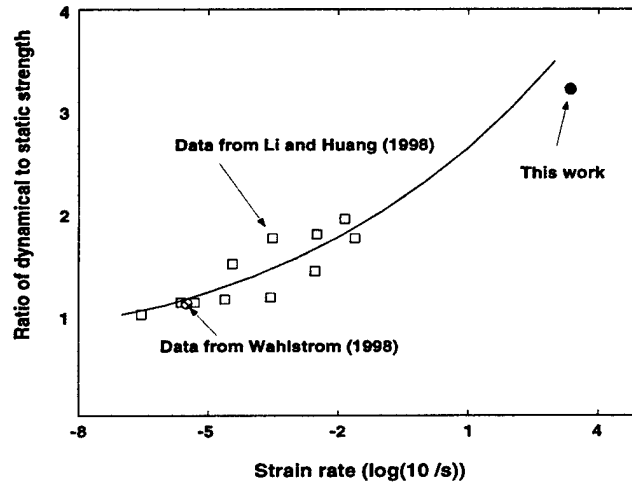


Figure 10: Unconfined compressive strength versus strain rate. The solid line is from Eq. (10). In order to compare strengths at a referenced strain rate of  $3 \times 10^{-7}/s$  (static), the unconfined compressive strength of G-mixture mortar at  $2.8 \times 10^{-7}/s$  is estimated as  $\sigma_f^0 = 0.042$  GPa using Eq. (10). This value of  $\sigma_f^0$  is used as a normalization factor for the G-mixture mortar.

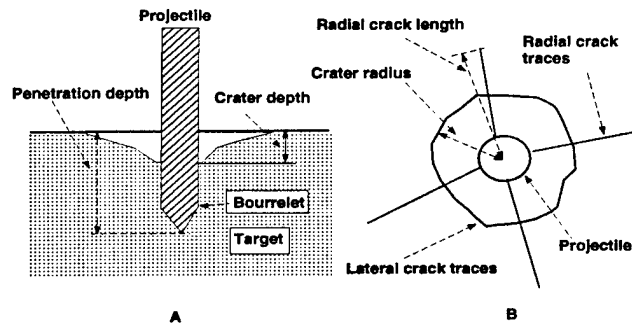


Figure 11: Schematic view of post-shot targets. A is side-view and B is top-view.

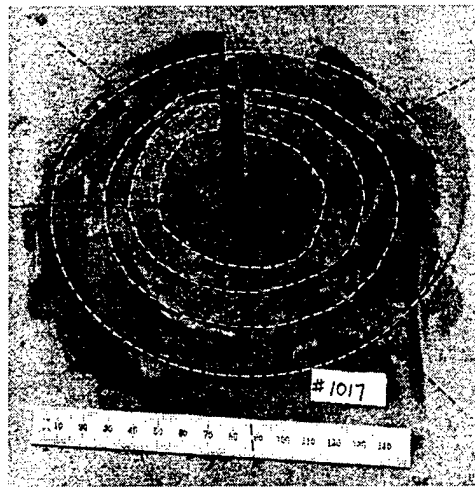


Figure 12: Damage pattern of Shot 1017 target. Black lines are traces of radial cracks. White lines are traces of lateral cracks. Spall fragments from the target were reconstructed after the experiment.

that penetration damage to target materials away from the penetration path is via two types of cracks, i.e., radial and lateral cracks.

**Radial cracks:** The typical appearance of radial cracks on the impact surface is shown in Figure 12. Usually between 4 and 8 radial cracks appeared on the impact surface. These radial cracks with different lengths seem to have propagated along radii from the impact site. Figure 13 shows the radial crack length measured on the impact surface as a function of initial projectile energy. Because all crack lengths were measured one or two days after the experiments were conducted, it is possible that the crack length increased after the impact as a result of residual stresses.

Figure 13 demonstrates a correlation between radial crack length and initial projectile energy for the experiments in which the targets were cratered but intact after impact. For Shots 1018 and 1035, radial cracks propagated both to the lateral target surface and down inside the target. The radial crack length down inside target is much longer than the penetration depth. The final penetration depth of Shot 1035 is 78 mm but the height of the radial cracks is ~ 200 mm. The whole target of Shot 1018 was shattered by radial and lateral cracks but the final penetration depth was only 179 mm. These experimental results indicate that radial cracks propagated at a velocity that is much faster than the penetration velocity during penetration and damaged a much larger region of the target materials than the penetration process itself did. Therefore, it is very important to consider the radial crack damage region in applications of penetrators to space missions.

**Lateral cracks and crater profiles** Figure 12 demonstrate that the trace



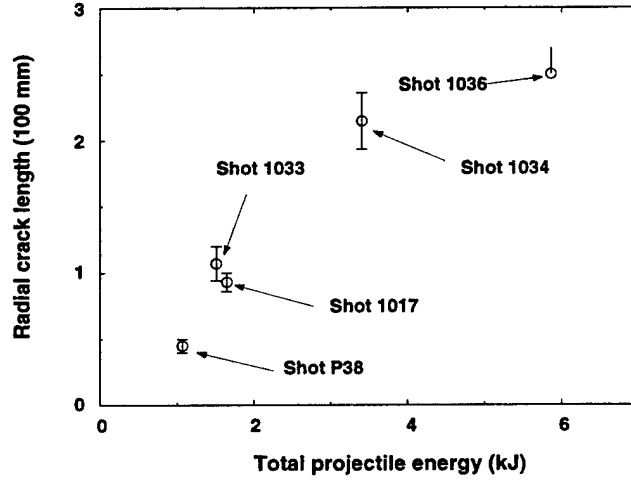


Figure 13: Radial crack length versus impact energy. Cracks of Shot 1036 reached the target edge along the radial direction on the impact surface, and therefore were probably stopped prematurely.

of lateral cracks on the impact surface is close to circular and the spacing of lateral cracks increases away from the impact site. Figure 14 shows final crater profiles measured on the recovered targets. The final crater profiles are believed to be formed by the last lateral crack that propagated to impact the free surface during penetration. Crater profiles have several similar features: (1) A small plateau appears at the bottom of penetration (Part I in Figure 14). The plateau width increases with final penetration depth. This zone may represent mortar comminuted during penetration; (2) The crater wall is falling steep in a region between  $\sim 60^\circ$  and  $\sim 20^\circ$  from the impact surface (Part II in Figure 14). The slope of the crater wall in this region increases with final penetration depth; (3) Another plateau or region of low slope on the crater wall is between  $\sim 20^\circ$  and  $\sim 16^\circ$  from the impact surface (Part III in Figure 14); (4) The crater wall gets steeper again in a region between  $\sim 16^\circ$  and  $\sim 0^\circ$  from the impact surface (Part IV in Figure 14); (5) Figure 15 shows the relation between the ratio of crater radius to projectile radius and initial projectile velocity. It seems that the ratio is correlated with impact velocity. (6) Figure 16 shows that the crater depth,  $d_c$ , is linearly proportional to the initial projectile energy,  $E_i$ , as

$$d_c = (2.4 \pm 0.6) + (7.27 \pm 0.19)E_i, \quad (13)$$

where  $d_c$  is in mm and  $E_i = mv^2/2$  is in kJ. Because crater profiles reflect lateral crack propagation during penetration, study of these features would help to understand the formation and propagation of lateral cracks during penetration.

Because the radial cracks on impact surface were traced back to impact site on the recovered fragments induced by the lateral cracks, the radial cracks

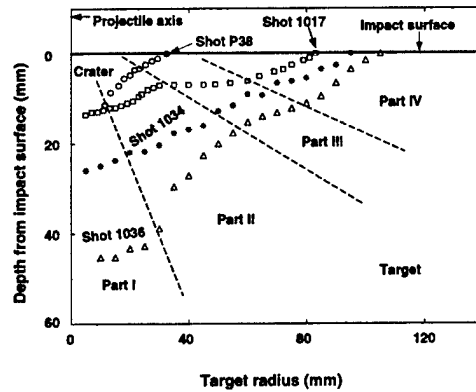


Figure 14: Crater profiles of Shots P38, 1017, 1034 and 1036.

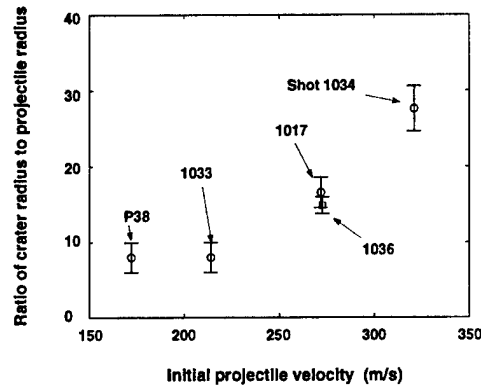


Figure 15: Ratio of crater-to-projectile radius versus initial projectile velocity.

formed earlier than the lateral cracks.

**Damage inside target materials** In order to investigate post-shot target material damage around the penetrated regime inside recovered targets, the targets for Shots 1017 and P38 were sectioned along the impact axis. Crater and damage patterns from these cross-sections are shown in Figures 17 and 18. Figure 19 schematically shows the damage pattern and some of the tensile (spall) fractures inside the target of Shot 1017. The cross-sections clearly show that there are no visible cracks just in front of the penetrator. The micro-structure of mortar near and far away from the bottom of the penetration does not show any visible cracks ([17]). The mortar density, and P- and S-wave velocity versus distance from the bottom of the penetration measured on the recovered targets ([17]) suggest that the mortar in front of the penetration was compacted during penetration. In addition, Figure 17 demonstrates that lateral cracks originated

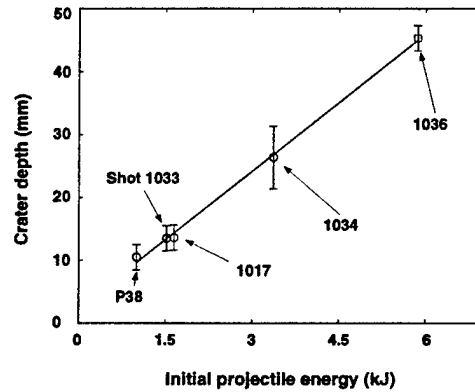


Figure 16: Crater depth versus initial projectile energy. Solid line is linear fit (Eq. (13)).

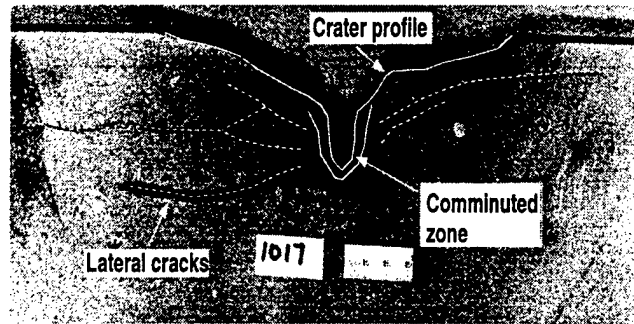


Figure 17: Cross-section of the recovered target for Shot 1017. Water was used to increase the contrast between the damaged and undamaged regions.

only from the region around penetration path, not from the region just in front of the penetration. These results seem to support that damage in front of a penetrator in mortar is via compaction.

### 3.2.2 Projectile damage pattern

The damage to the lateral surface of the projectile reflects the degree of contact between projectile and target materials during penetration. Figure 20 shows two recovered projectiles. Two parameters related to projectile surface conditions are investigated on the recovered projectiles. They are defined: (1) Ink damage length  $L_i$ : This is measured from the projectile bourrelet (defined in Figure 11) to the point at which ink was cleaned but no visible erosion occurred on the projectile surface during penetration. This length only reflects that very light

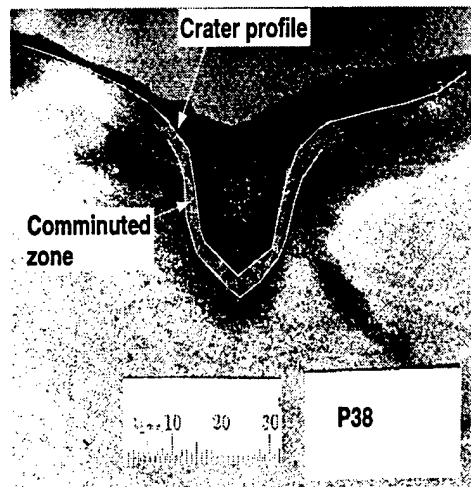


Figure 18: Cross-section of the recovered target for Shot P38.

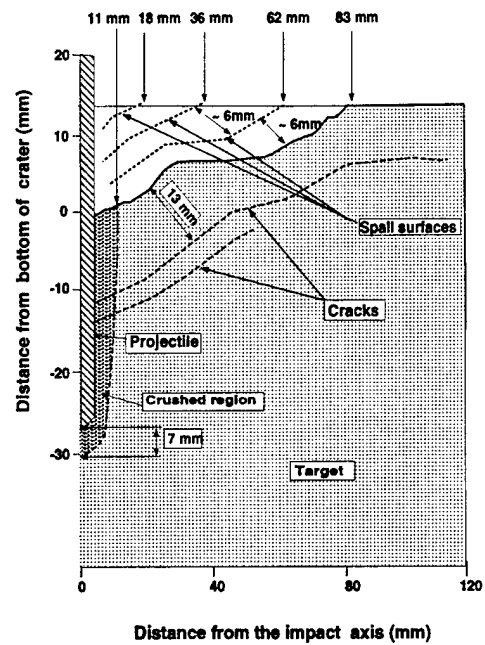


Figure 19: Schematic of cross-section of the target for Shot 1017.

contact between projectile and target materials occurred in this area during penetration; (2) Projectile lateral surface damage length  $L_d$ : This is measured from the projectile bourrelet to the point at which the projectile surface was eroded by aggregates in the mortar during penetration. This length provides the area in which the projectile surface was in contact with target material under a certain normal pressure during penetration.

For Shot P38, the ink on the projectile lateral surface was nearly untouched by the target materials during penetration. For all the other experiments, various values of  $L_i$  and  $L_d$  are observed on recovered projectile surfaces. Figure 21 shows the same damage lengths (normalized by final penetration depth) versus final penetration depth. These results demonstrate that (1)  $L_d$  is very short, < 20% of final penetration depth of the experiments with an intact target after impact. Therefore, frictional effects on the projectile lateral surface can be approximately ignored for an approximate analytic model to describe rigid body penetration into brittle materials under the conditions similar to the present experiments, and (2) for this projectile shape, it is very difficult to deploy an anchor into brittle materials because penetrators only have contact with less than 20 % of the final penetration depth.

The damage to the projectile head surface records the friction or temperature history effect on the surface during penetration. From the recovered projectiles, roughness of the projectile head surface increases with initial impact velocity. Due to the difficulty of measuring roughness on a non-planar surface, I do not show any direct data on the roughness here. However, the variation of projectile diameter at the bourrelet gives a certain degree of representation of the roughness on projectile head surface. Comparison of the projectile diameter measured before and after impact (Table 1) shows that the ratio of projectile diameter after impact to the diameter before impact decreases with impact velocity. Therefore, the roughness of the projectile head surface increases with impact velocity.

### 3.3 Penetration time history data and scaling

In this part, we discuss the experimental data on final penetration depth, energy per penetration unit volume, target dimension effects, penetration duration, penetration depth-time history, and we deduce the penetration velocity- and deceleration-time history. These parameters provide information on different aspects of the penetration process.

#### 3.3.1 Final penetration depth

The relation between final penetration depth and initial projectile parameters is very important for all applications. For the present experiments, the parameters that were varied are projectile velocity, projectile dimensions (diameter and length) and projectile mass. The experimental data (Table 1) yield a good linear relation between final penetration depth,  $P_{max}$ , and impact energy per unit cross-section area,  $e_s = mv^2/(2\pi R^2)$ , for the experiments with intact targets

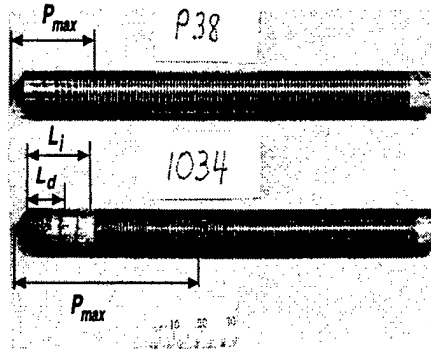


Figure 20: Recovered projectiles.  $P_{max}$  is the final penetration depth.  $L_i$  is the ink damage length.  $L_d$  is the projectile lateral surface damage length.

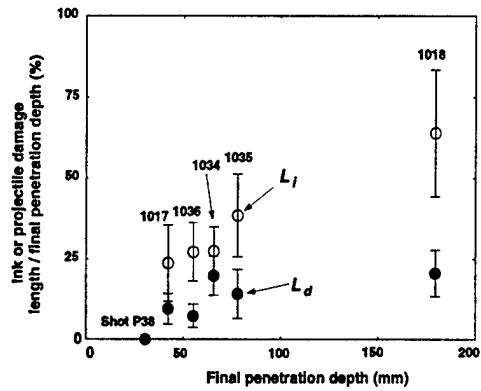


Figure 21: Normalized damage length versus final penetration depth.

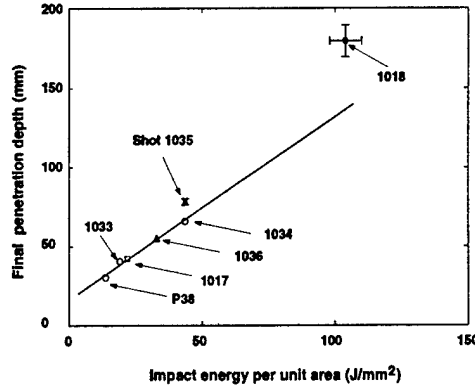


Figure 22: Final penetration depth versus initial impact energy per unit cross-section area. Solid line is linear fit to the data (Eq. (14)).

after impact (Figure 22). A best fit to the experimental data yields

$$P_{max} = (1.15 \pm 0.08)e_s + (16.39 \pm 2.17), \quad (14)$$

where  $P_{max}$  is in mm and  $e_s$  is in  $\text{J/mm}^2$ . Because the two coefficients in Eq. (14) depend on target material properties, friction coefficient, projectile head shape etc., this scaling relation is only true for the same target material under the same projectile shape and rigid body assumption.

### 3.3.2 Energy per unit penetration volume

The impact energy required to open unit penetration volume reflects the resistance of the target material to penetration. It relates to target material strength and its rate dependence, friction coefficient, wave generation and crack propagation during penetration. In order to estimate this parameter, total penetration volume,  $Vol$ , is defined as

$$Vol = \pi R^2(P_{max} - R) + \frac{\pi}{3}R^3 = \pi R^2(P_{max} - \frac{2}{3}R), \quad (15)$$

where the term  $\pi R^2/3$  is the volume of the conical head of the projectile. Then, energy per unit penetration volume,  $e_v$ , is

$$e_v = \frac{\frac{1}{2}mv^2}{Vol} = \frac{e_s}{P_{max} - \frac{2}{3}R}. \quad (16)$$

Based on the experimental data,  $e_v$  is given in Figure 23. It shows that  $e_v$  increases from  $0.5 \text{ J/mm}^3$  at  $e_s = \sim 15 \text{ J/mm}^2$  to  $\sim 0.7 \text{ J/mm}^3$  at  $e_s = \sim 45 \text{ J/mm}^2$ . Substituting Eq. (14) into Eq. (16),  $e_v$  is a function of  $e_s$  as

$$e_v = \frac{e_s}{(1.15 \pm 0.08)e_s + (16.39 \pm 2.17) - \frac{2}{3}R}, \quad (17)$$

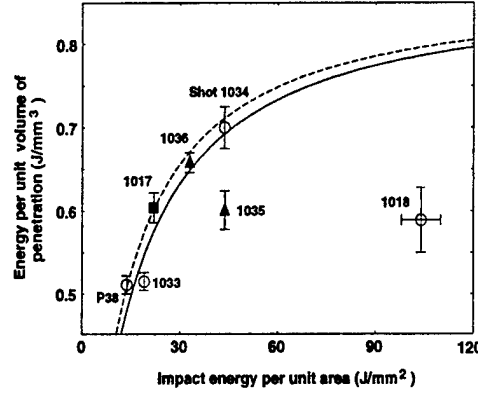


Figure 23: Energy per unit penetration volume versus impact energy per unit cross-section area. Dashed and solid lines are calculated from Eq. (17) for projectiles with 15 and 10 mm diameters, respectively.

where  $e_v$  is in  $\text{J/mm}^3$ ,  $e_s$  is in  $\text{J/mm}^2$  and  $R$  is in mm. The calculated results for 10 and 15 mm diameter projectiles are also given in Figure 23. From Figure 23,  $\partial e_v / \partial e_s$  decreases with increasing  $e_s$ .

$e_v$  also represents average pressure acting on the target material in the spot beneath the penetrator during penetration. This pressure includes all contributions from wave generation, material strength and its strain rate dependence and also friction. Figure 23 demonstrates that averaged pressure acting on the projectile is 0.5 GPa at  $e_s = \sim 15 \text{ J/mm}^2$  and 0.7 GPa at  $e_s = \sim 45 \text{ J/mm}^2$  ( $\text{J/mm}^3 \sim \text{GPa}$ ). These values are  $\sim 10$  to  $20$  times higher than the resistance pressure expected based on unconfined strength tests of the G-mixture mortar (0.04 GPa under quasi-static loading ([29])) and  $\sim 6$  to  $8$  times higher than the resistance pressure due to the mortar unconfined strength expected from the Hugoniot elastic limit (Figure 10). If it is assumed that friction coefficient is 1, the measured averaged pressure is still  $\sim 3$  to  $4$  times higher than the possible highest averaged pressure just due to mortar strength and its rate dependence. Therefore, the dependence of material strength on strain rate and the friction effect alone can account for less half of the estimated energy consumed during penetration. This result demonstrates that wave generation may be the dominant process during rigid body penetration into brittle materials.

### 3.3.3 Effects of target dimension on penetration

Scaling relations based on experimental data are always used to predict penetration parameters in various applications in which target dimensions are much larger than targets used in laboratory experiments. Therefore, the effect of target dimension on penetration parameters should be considered properly in order to give reasonable predictions.



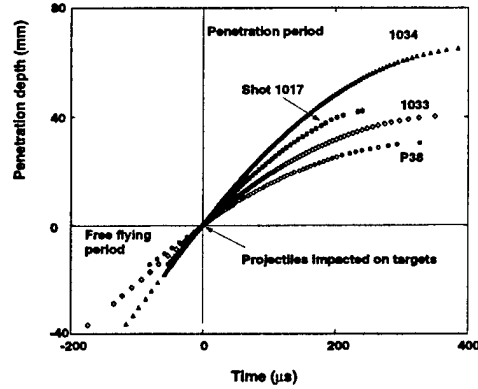


Figure 24: Penetration depth versus time.

For brittle target materials, finite dimensions affect penetration processes via two ways: interactions between the wave generated from penetration and the free surface, and also cracks generated during penetration which may reach the free surface. Figure 23 demonstrates that interaction between cracks and the free surface has significant effects on penetration under the present experimental conditions because  $e_v$  for the experiments in which targets were intact after impact (Shots P38, 1017, 1033, 1034 and 1036) is much higher than  $e_v$  for the experiments in which targets were broken into pieces (Shots 1018 and 1035) during penetration. Therefore, in order to avoid data contamination from crack propagation in brittle materials, an upper limit to the initial projectile velocity must be determined based on target dimensions. Because target dimension effects on penetration come from crack propagation through the target, the method used to encapsulate brittle target materials with a cylindrical steel shell to eliminate finite dimension effects appears to be difficult to rationalize.

For a mortar target with a diameter of 500 mm, the finite dimensions will significantly affect the penetration when the velocity of 10 (15) mm diameter and 150 mm length projectiles is above 350 (280) m/s, based on the present experiments.

#### 3.3.4 Penetration time history

The penetration time history is important for both applications and understanding of the penetration process itself because it provides detailed information on the interaction between the projectile and target materials during penetration. In the following, experimental data on penetration depth-time histories is presented first, and then the deduced parameters are discussed in detail. Penetration depth-time histories obtained from the experiments are given in Figure 24. Penetration durations,  $t_{max}$ , are listed in Table 1.

**Penetration duration** Penetration duration is one of important parameters in penetration dynamics because it provides the time constraints on theoretical models and practical applications. Due to the difficulty in measuring it, no empirical scaling relation has been published and only a few very scattered data are available for very large dimension experiments on soil targets([13]). In general, the duration of penetration depends on initial velocity, target materials, and projectile dimensions. Based on the present results, we only discuss the effects of initial velocity and projectile dimension on penetration duration.

Figure 25 gives the experimental data on penetration duration versus  $e_s$ . The experimental results demonstrate: (1) Penetration duration increases very slowly with the  $e_s$  for projectiles with same length; (2) The large difference between penetration durations for Shot 1017 and 1033 shows that penetration duration is very sensitive to projectile length; (3) Projectile diameter does not play an important role in changing penetration duration if mass per unit cross-section area is approximately constant ( $0.86 \text{ g/mm}^2$  for 10 mm diameter projectiles and  $0.89 \text{ g/mm}^2$  for 15 mm diameter projectiles).

Based on the experimental data, the penetration duration  $t_{max}$  for the experiments with the same projectile length is linearly proportional to  $e_s$  (Figure 25). A best fit to the data yields

$$t_{max} = (2.08 \pm 0.25)e_s + (303.64 \pm 8.04), \quad (18)$$

where  $t_{max}$  is in  $\mu\text{s}$  and  $e_s$  is in  $\text{J/mm}^2$ . As mentioned above, penetration duration is not sensitive to  $e_s$ , e.g.,  $t_{max}$  only changes  $\sim 25\%$  while  $e_s$  increases by 4 times ( $t_{max} = 324.4$  and  $407 \mu\text{s}$  at  $e_s = 10$  and  $50 \text{ J/mm}^2$ , respectively).

Based on Eq. (18) and the fact that penetration duration is approximately independent of projectile diameter, penetration duration is believed to be mainly controlled by projectile mass per unit cross-section area,  $m_m = m/(\pi R^2)$ . In addition, the penetration duration of Shot 1017 is much shorter than that of Shot 1033 although  $e_s$  is approximately the same ( $e_s$  is 22 and 19  $\text{J/mm}^2$  for Shot 1017 and 1033, respectively). Therefore it is believed that the dependence of  $t_{max}$  on  $m_m$  should be reflected by the second term in Eq. (18). As an estimation, the second term is assumed to be linearly proportional to  $m_m$  and Eq. (18) is rewritten as

$$t_{max} = (2.08 \pm 0.25)e_s + (349.0 \times m_m \pm 8.04), \quad (19)$$

where  $m_m$  is in  $\text{g/mm}^2$ .  $t_{max}$  is calculated to be  $253.4 \mu\text{s}$  using Eq. (19) for the conditions of Shot 1017 ( $e_s = 22 \text{ J/mm}^2$  and  $m_m = 0.595 \text{ g/mm}^2$ ). The predicted penetration duration is in good agreement with the measured penetration duration ( $240 \mu\text{s}$ ). Therefore, Eq. (19) approximately gives the scaling rule of penetration duration under the present experimental conditions.

**Penetration velocity-time history** The penetration velocity time-history is deduced by differentiating a tenth-degree polynomial that fits measured penetration depth-time history data for each experiment. The deduced velocity-time histories (Figure 26) are divided into three stages as: (1) Initial

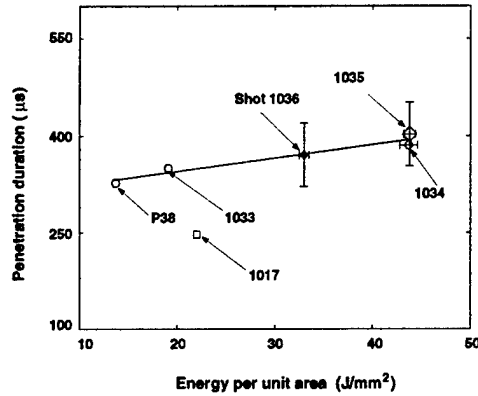


Figure 25: Penetration duration versus energy per unit area. Solid line is linear fit (Eq. (18)).

penetration stage: In this stage, the projectile velocity did not change significantly during a short period ( $\sim 20 \mu\text{s}$ ) just after the projectile impacted the target. This is due to both the rigid body assumption (velocity change on impact surface needs some time ( $\sim 10 \mu\text{s}$ ) to affect the velocity at measurement location) and the very small contact area between the projectile head and the target material during the initial penetration; (2) Steady penetration stage: In this stage, the projectile was under a relatively long and steady deceleration period. The duration of this period is  $\sim 276, 170, 325$  and  $318 \mu\text{s}$  for Shots P38, 1017, 1033 and 1034, respectively; (3) Penetration stop stage: When projectile velocity decreased to a critical value, projectile deceleration increased and penetration stopped suddenly. The critical velocity is  $\sim 37, 37, 18$  and  $49 \text{ m/s}$  for Shots P38, 1017, 1033 and 1034, respectively. The average critical velocity for projectiles with 150 mm length and 10 mm diameter is  $(35 \pm 15) \text{ m/s}$ .

**Penetration deceleration-time history** In order to deduce the deceleration from the measured penetration depth-time history, the tenth-order polynomial was differentiated twice. But the result was very noisy generally because the second differentiation magnifies the minor misfit of the polynomial to the data and measurement errors. The best deceleration time-history deduced is for Shot 1033 as shown in Figure 27. The features of deduced deceleration time history are (1) deceleration increases rapidly from 0 to about  $7 \times 10^4 \text{ g}$  in the first  $\sim 40 \mu\text{s}$ , (2) deceleration slowly decreases from  $7 \times 10^4 \text{ g}$  to  $\sim 5.5 \times 10^4 \text{ g}$  in about  $270 \mu\text{s}$  and (3) deceleration jumps up again when penetration is close to stopping.

In order to estimate average deceleration amplitude during penetration, penetration velocity in the steady penetration stage is assumed to decrease linearly with time (Figure 26). Then, the average deceleration obtained is shown in Figure 28. The results demonstrate that the average deceleration,  $\bar{a}$ , in the steady penetration stage for projectiles with same length is linearly proportional to

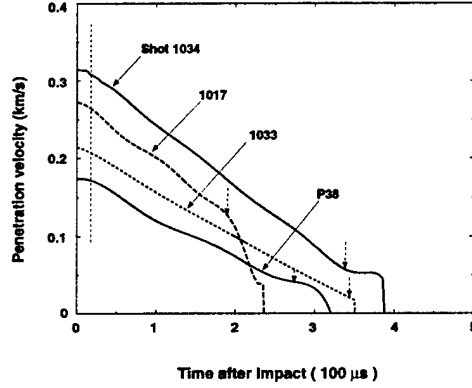


Figure 26: Deduced penetration velocity-time history. The initial penetration stage is between the vertical dashed line and zero time (impact time). The steady penetration stage is between the vertical dashed line and the vertical arrow. The penetration stop stage is beyond the vertical arrow.

initial impact velocity. A best fit to the data for projectiles with same length yields:

$$\bar{a} = 192.4v + 1.89 \times 10^4, \quad (20)$$

where  $\bar{a}$  is in g, and  $v$  is in m/s.

Eq. (20) can be used to estimate averaged pressure acting target materials during steady penetration. Assuming that friction force on projectile lateral surface is ignored as discussed in previous section, for a conical projectile, pressure normal to the projectile cone surface,  $\sigma$ , is ([18])

$$\sigma = \frac{m\bar{a}}{\sqrt{2}\pi R^2(\eta \cos(\theta) + \sin(\theta))}, \quad (21)$$

where  $\eta$  is the friction coefficient and  $\theta$  is the half-cone angle. The possible value of  $\eta$  ranges from 0 to 1. Therefore, upper and lower limit of  $\sigma$  is estimated when  $\eta = 0$  and 1, respectively as shown in Figure 29. This estimated results once again show that resistance pressure acting on projectile surface is about 2 to 4 times higher than the possible highest pressure induced only by friction and material strength and its strain rate effect. In order to estimate average shock wave pressure generated by the penetration in target materials, particle velocity is assumed to be half of initial impact velocity. Then average shock wave pressure is calculated using Eq. (10). The average shock wave pressure (Figure 29) is very comparable with the average pressure acting on projectile surface. Therefore, this result strongly supports that shock wave generation is the dominant process during rigid body penetration into brittle materials under present experimental conditions.

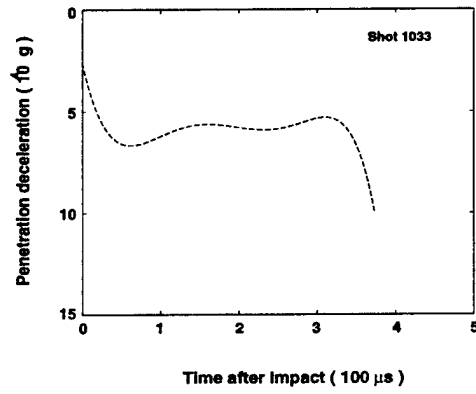


Figure 27: Deduced deceleration-time history.

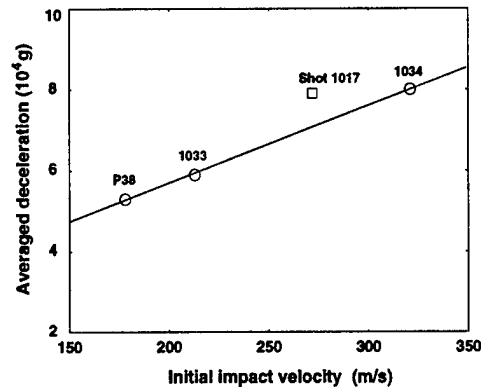


Figure 28: Average deceleration versus initial impact velocity. Solid line is linear fit to the data of Shots P38, 1033 and 1034 (Eq. (20)).

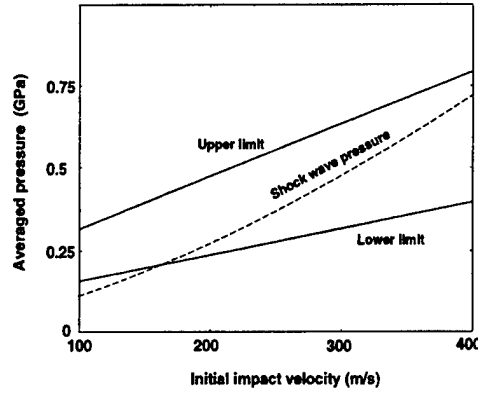


Figure 29: Average pressure normal to projectile surface versus initial impact velocity. Upper and lower solid lines are calculated using Eq. (21) with  $\eta = 0$  and 1, respectively. Dashed line is calculated using the Hugoniot relation of [23] under the assumption that the average particle velocity in G-mixture mortar is half of the initial impact velocity.

### 3.3.5 Penetration process similarity

The purpose to investigate the similarity among penetration time histories under different initial conditions is to see if any scaling relation for penetration time histories exists. Figure 30 shows all the experimental data of penetration depth time history normalized by final penetration depth versus penetration time normalized by penetration duration. It demonstrates a very strong penetration process similarity among the experimental data of Shots P38, 1033 and 1034. These experiments have same projectile length and diameter. The relation between the normalized penetration depth versus the normalized penetration time is fully similar with each other in whole penetration process. This result suggests that a scaling relation for penetration process with same projectile dimensions exists as

$$\frac{P(t, v)}{P_{max}} = f\left(\frac{t}{t_{max}}\right), \quad (22)$$

where  $f$  is a function of  $t/t_{max}$ .  $f$  can be determined by polynomial fit to the data of the three experiments (Shots P38, 1033 and 1034). Then, the scaling relation of penetration depth time history is

$$P(t, v) = P_{max} f\left(\frac{t}{t_{max}}\right). \quad (23)$$

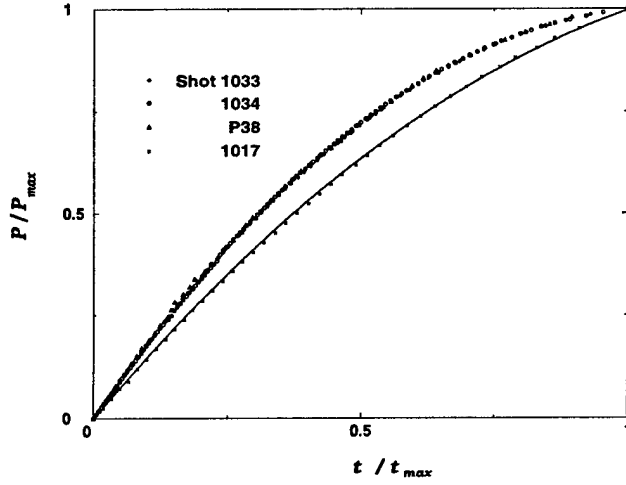


Figure 30: Normalized penetration depth versus normalized penetration time. Solid line is penetration depth-time history for Shot 1017 predicted using Eq. (24).

Substituting  $P_{max}$  and  $t_{max}$  with Eq. (14) and (19), respectively, the scaling relation is

$$P(t, v) = ((1.15 \pm 0.08)e_s + (16.39 \pm 2.17))f\left(\frac{t}{(2.08 \pm 0.25)e_s + (349.0 \times m_m \pm 8.04)}\right). \quad (24)$$

If the projectile dimension effect has been included in  $e_s$  and  $m_m$ , Eq. (24) can be used to predict penetration depth-time history under different initial conditions. Using Eq. (24), the predicted penetration depth time history of Shot 1017 is in a very good agreement with the experimental data as shown Figure (30). Based on this figure, projectile dimension effect on penetration process seems to be included in  $e_s$  and  $m_m$ . Therefore, Eq. (24) can be used to scale penetration depth-time history under different initial conditions for rigid body penetration into G-mortar target. Also, Eq. (24) predicts that average deceleration of projectiles increases with projectile length, this is confirmed by the experimental results shown in Figure 28. However, I must mention that the above conclusion is only based on the experimental data under two projectile lengths, and more experiments are needed to verify it.

### 3.4 Comparisons among empirical relations

Sandia National Laboratories ([13]) suggested an empirical relation between final penetration depth and initial projectile parameters as

$$P_{max} = 1.14 \times 10^{-6} S \times N \frac{m}{A} (v_0 - 100), \quad (25)$$

where  $S$  and  $N$  are defined as target penetrability number (a measure of rock resistance) and projectile nose performance coefficient. Although Eq. (25) includes two dimensionless empirical parameters, they are equivalent to one parameter. The averaged value of  $S \times N$  determined from the present data is  $S \times N = 0.353 \pm 0.035$ . The predicted final penetration depth using Eq. (25) is shown in Figure 31.

Army's Waterways Experiment Station ([13]) suggested an empirical relation for conical projectile as

$$P_{max} = \frac{M}{A} \frac{N_{rc}}{\rho} \left[ \frac{v_0}{3} \left( \frac{\rho}{\sigma_{cr}} \right)^{0.5} - \frac{4}{9} \ln \left( 1 + \frac{3v_0}{4} \left( \frac{\rho}{\sigma_{cr}} \right)^{0.5} \right) \right], \quad (26)$$

where  $\rho$  is target material density, and  $N_{rc} = 0.805 \sin^{-0.5}(\theta)$ ,  $\sigma_{rc} = \sigma_f \left( \frac{RQD}{100} \right)^{0.2}$ . Because the projectiles used in the present experiments had conical head with half-angle  $45^\circ$ ,  $N_{rc} = 0.957$ . Only one parameter,  $\sigma_{rc}$ , needs to be determined empirically. Based on the present experimental data, the average value of  $\sigma_{rc}$  is  $\sigma_{rc} = 81.5 \pm 9$ , (MPa). The predicted final penetration depth is shown in Figure 31. From the definition of RQD ([13]), the value of RQD must be  $< 100$  for any materials with pre-existed micro-cracks, cavities etc. because RQD = 100 is for perfect target materials. However, RQD is deduced to be 2060 when  $\sigma_f = 44.5$  MPa for the G-mixture mortar.

[7] suggested that the final penetration depth of a projectile with a ogive nose is

$$P_{max} = \frac{m}{2A\rho z} \ln \left( 1 + \frac{\rho v_1^2 z}{B} \right) + 4R, \quad P_{max} > 4R, \quad (27)$$

$B$  is a empirical constant. where  $v_1$  and  $z$  are defined as  $v_1^2 = v_0^2 - \frac{4\pi R^3 B}{m}$ ,  $z = \frac{4R_o R - R^2}{6R_o}$ , where  $R_o$  is ogive head radius. For a conical projectile,  $z = 0$  because  $R_o$  is infinite. Therefore, Eq. (27) can not be used for a conical projectile directly. However the first term of the right-hand-side of Eq. (27) is 0/0 type when  $z \rightarrow 0$ , the limit of the right-hand-side is

$$\lim_{z \rightarrow 0} P_{max} = \frac{mv_1^2}{2AB} + 4R. \quad (28)$$

Using the definition of  $v_1$ , the above equation is

$$P_{max} = \frac{mv_0^2}{2AB} + R \left( 4 - \frac{2}{\pi} \right). \quad (29)$$

The averaged value of  $B$  is determined to be  $(9.3 \pm 1.1) \times 10^8$  (J/m<sup>3</sup>). The predicted final penetration depth is given in Figure 32.

Figures 31 and 32 demonstrate that all the three expressions discussed above give reasonable prediction of final penetration depth under the present experimental conditions. Eq. (25) predicts that final penetration depth is linearly proportional to impact momentum per unit cross-section area, and Eq. (26) also predicts the same relation when initial impact velocity is not very high



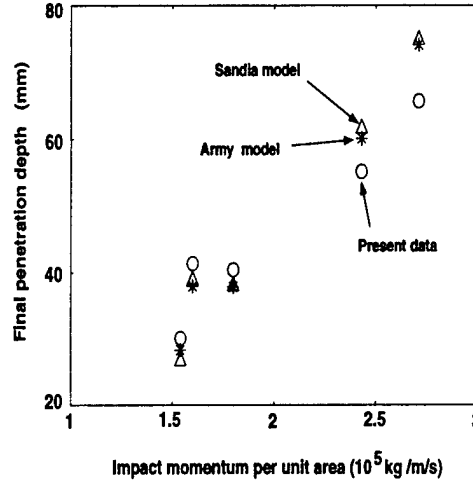


Figure 31: Final penetration depth versus impact momentum per unit area.

(say,  $v_0 < 4(\sigma_{cr}/\rho)^{0.5}/3$ , that is  $\sim 280 \text{ m/s}$  under the present experimental conditions). Eq. (29) predicts that final penetration depth is linearly proportional to impact energy per unit cross-section area. However, the present experimental data show that the final penetration depth is linearly proportional to the impact energy per unit cross-section area. Therefore, the present experimental data support the linear relationship between final penetration depth and impact energy per unit area.

## 4 Conclusions

Based on the experimental data, we conclude:

(1) A penetration depth time history measuremental method was developed. For the first time, whole penetration depth-time history was recorded with very dense datum point under  $10^5 \text{ g}$  deceleration. The results provide dynamic constraints to theoretic models, specially numerical simulations.

(2) The non-dispersive Hugoniot elastic wave in the G-mixture has an amplitude of  $\sim 0.14 \text{ GPa}$  and a velocity of  $\sim 4.3 \text{ km/s}$ . The amplitude of the dispersive elastic wave is about  $0.1 \text{ GPa}$  under the peak shock wave pressure of  $\sim 1 \text{ GPa}$ . The present experimental data show that the Hugoniot relation of [23] can be used to approximately describe the G-mixture mortar response to shock loading.

(3) The target materials are damaged via compacting in the region in front of penetrators and via brittle radial and lateral cracks propagations in the region surrounding penetration path. Macro-cracks just in front of penetrators as suggested by [9] and [5] were not produced in the material studied here. Ra-

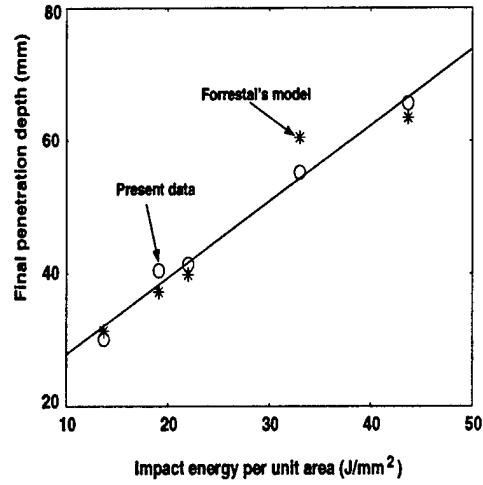


Figure 32: Final penetration depth versus impact energy per unit area. Solid line is Eq. (14).

dial crack traces on impact surface are very straight along radial from impact site. Radial crack length appearing on impact surface is correlated with initial projectile energy. Lateral cracks have circular trace on impact surface. The distance between two adjacent lateral cracks increases with the distance from impact site. Lateral cracks follow a very complex propagation path given by crater profiles. Crack surface morphology looks similar to that of the radial cracks and seems to be tensile cracks.

(4) Energy needed to create unit penetration volume is found to be increase with impact velocity or penetration depth for the experiments in which targets were still intact after impact. Based on average value of energy per unit penetration volume, average pressure acting on target material during penetration is found to be 10 to 20 times higher than that due to strength of target materials under quasi-static loading. The interaction between cracks and target free surface significantly affects rigid body penetration into brittle materials based on present data.

(5) The contact length on projectile lateral surface between projectile and target materials during penetration is  $< 20\%$  of final penetration depth. This result suggests that lateral friction effect on penetration process can be approximately ignored, and shows the difficulty to employ penetrators into brittle materials as anchors. The roughness of projectile head surfaces increases with penetration velocity. This reflects friction (temperature) effects on projectile head surface.

(6) Final penetration depth,  $P_{max}$ , is linearly scaled with initial projectile energy per unit cross-section area,  $e_s$ , for projectiles with same projectile head shape, different length and diameter when targets are intact after impact

(Eq. (14)). Penetration duration,  $t_{max}$ , is found to scale linearly with  $e_s$  for projectiles with same length and different diameters (Eq. (18)). Therefore, penetration duration dependence on projectile length is suggested to be described by Eq. (19). The prediction from this relation is in good agreement with the experimental data under different projectile length.

(7) Deduced penetration velocity time histories suggest that whole penetration history is divided into three stages: (1) initial stage in which projectile velocity change is small due to very small contact between projectile and target materials, (2) steady penetration stage in which projectile velocity continues to decrease smoothly, (3) penetration stop stage in which projectile deceleration jump up when velocities is close to a critical value that is  $\sim 35$  m/s from the experiments. Deduced average deceleration in the steady penetration stage is found to be linearly proportional to initial impact velocity when projectiles have the same dimensions (Eq. (20)). Average pressure acting on target materials during penetration is estimated to be very comparable with shock wave pressure. This result suggests that shock wave generation is the dominant process for energy exchanging between projectile and target materials during penetration.

(8) The experimental data of penetration depth-time histories suggest that a penetration process similarity between normalized penetration depth,  $P/P_{max}$ , and normalized penetration time,  $t/t_{max}$ , exists (Eq. (24)). This similarity can be used to predict the penetration depth time history of projectiles with different initial conditions.

## References

- [1] Ahrens, T. J., Equation of state, *High-Pressure Shock Compressions of Solids*, edited by J. R. Asay and M. Shahinpoor, published by Springer-Verlag, New York, 75-114, 1993.
- [2] Ahrens, T. J., Champollion physical properties probe and sample acquisition and transfer mechanism, *Proposal for Rosetta Mission*, 1995.
- [3] Anderson, W. W., T. J. Ahrens, A. Gibson, R. Scott, and K. Suzuki, Emplacement of penetrators into planetary surfaces, *J. Geophys. Res.*, 101, 21,137-21,149, 1996.
- [4] Backman, M. E. and W. Goldsmith, The mechanics of penetration of projectile into targets, *Int. J. Engng. Sci.*, 16, 1-99, 1978.
- [5] Bless, S. J., J. P. Barber, R. S. Bertke and H. F. Swift, Penetration mechanics of yawed rods, *Int. J. Eng. Sci.*, 16, 829-834, 1978.
- [6] Corbett, G. G, S. R. Reid, and W. Johnson, Impact loading of plates and shells by free-flying projectiles: A review, *Int. J. Impact Engng*, 18, 141-230, 1996.
- [7] Forrestal, M. J., Penetration into dry porous rock, *Int. J. Solids Structure*, 22, 1485-1500, 1986.

- [8] Forrestal, M. J. and V. K. Luk, Penetration into soil targets, *Int. J. Impact Engng.*, Vol. 12, 427-444, 1992.
- [9] Forrestal M. J. and D. Y. Tzou, A spherical cavity-expansion penetration model for concrete targets, to appear in *Int. J. Solids Struct.*, 1998.
- [10] Gavit, S. A and G. Powell, The new millennium programs Mars microprobe mission, *Acta Astronautic*, 39, 273-280, 1996.
- [11] Goldsmith, W., Review non-ideal projectile impact on targets, *Int. J. Impact Engng.*, 22, 101-395, 1999.
- [12] Grady, D., Shock and release data for SAC-5 concrete to 25 GPa, Sandia National Laboratories Technical Memorandum-TMDG0595, October, 1995.
- [13] Heuze, F. E, An overview of projectile penetration into geological materials, with emphasis on rocks, *Int. J. Rock Mech. Min. Sci. & Geomech. Abstr.*, 27, 1-14, 1990.
- [14] Hohler, V. and A. J. Stilp, Long-rod penetration mechanics, *High Velocity Impact Dynamics*, edited by J. A. Zukas, published by John Wiley & Sons, Inc., New York, 321-404, 1990.
- [15] Levy, N. and W. Goldsmith, Normal impact and perforation of thin plates by hemispherically tipped projectiles, *Int. J. Impact Engng.*, 2, 209-229, 1984.
- [16] Li Zhaoxia and Yaoping Huang, Effect of strain rate on the compressive strength surface cracking and failure model of mortar, *ACI Material Journal*, 95, 512-518, 1998.
- [17] Liu, C., Brittle material response to shock loading, PhD Thesis, California Institute of Technology, 1999.
- [18] Liu, C. and T. J. Ahrens, Rigid body penetration dynamics: A simple analytic model, submitted to *Int. J. Impact Engng.*, 1999.
- [19] Masket, A. V., The measurement of forces resisting armor penetration, *J. Appl. Phys.*, 20, 132-140, 1949.
- [20] Marsh, S. P., *LASL shock Hugoniot data*, published by University of California Press, 1980.
- [21] Mizutani, H., Lunar interior exploration by Japanese lunar penetrator mission, LUNAR-A, *J. Phys. Earth*, 43, 657-670, 1995.
- [22] Persson, A., A theoretical and experimental study of rigid projectile penetration mechanics, *Proceedings of Second International Symposium on Ballistics*, Daytona Beach, FL., 1976.

- [23] Read, H. E. and C. J. Maiden, The dynamic behavior of concrete, *Systems, Science and Software Topical Report* 3SR-707, 1971.
- [24] Recht, R. F., High velocity impact dynamics: analytical modeling of plate penetration dynamics, *High Velocity Impact Dynamics*, edited by J. A. Zukas, published by John Wiley&Sons, Inc., 443-514, 1990.
- [25] Ross, C. A., P. Y. Thompson and J. W. Tedesco, Split-Hopkinson pressure-bar test on concrete and mortar in tension and compression, *ACI Materials Journal*, 86, 475-481, 1989.
- [26] Rubin, A. M., and T. J. Ahrens, Dynamic tensile failure induced velocity deficits in rock, *Geophys. Res. Lett.*, 18, 219-223, 1991.
- [27] Stilp, A. J. and V. Hohler, Experimental methods for terminal ballistics and impact physics, *High Velocity Impact Dynamics*, edited by J. A. Zukas, published by John Wiley& Sons, Inc., New York, 515-592, 1990.
- [28] Virostek, S. P., J. Dual and W. Goldsmith, Direct force measurement in normal and oblique impact of plates by projectiles, *Int. J. Impact Engng.*, 6, 247-269, 1987.
- [29] Wahlstrom, D., Compressive strength of G-mixture mortar and concrete, (letter), 1998.
- [30] Woodward, R. L., Material failure at high strain rates, *High Velocity Impact Dynamics*, edited by J. A. Zukas, published by John Wiley& Sons, Inc., New York, 65-107, 1990.
- [31] Wu E., H. Sheen, Y. Chen and L. Chang, Penetration force measurement of thin plates by laser Doppler anemometry, *Experimental Mechanics*, 34, 93-99, 1994.
- [32] Zhu G., W. Goldsmith and C. K. H. Dharan, Penetration of laminated Kevlar by projectiles-I. Experimental Investigation, *Int. J. Solids Structures*, 29, 399-420, 1992.
- [33] Zukas, J. A. and W. P. Walters, Analytical models for kinetic energy penetration, *High Velocity Impact Dynamics*, edited by J. A. Zukas, published by John Wiley& Sons, Inc., New York, 405-442, 1990.